PHYSICAL REVIEW E **66**, 066122 (2002)

Quasistatic brittle fracture in inhomogeneous media and iterated conformal maps: Modes I, II, and III

Felipe Barra,* Anders Levermann, and Itamar Procaccia
Department of Chemical Physics, The Weizmann Institute of Science, Rehovot, 76100, Israel

(Received 7 May 2002; published 18 December 2002)

The method of iterated conformal maps is developed for quasistatic fracture of brittle materials, for all modes of fracture. Previous theory, that was relevant for mode III only, is extended here to modes I and II. The latter require the solution of the bi-Laplace rather than the Laplace equation. For all cases we can consider quenched randomness in the brittle material itself, as well as randomness in the succession of fracture events. While mode III calls for the advance (in time) of one analytic function, modes I and II call for the advance of two analytic functions. This fundamental difference creates different stress distribution around the cracks. As a result the geometric characteristics of the cracks differ, putting mode III in a different class compared to modes I and II.

DOI: 10.1103/PhysRevE.66.066122 PACS number(s): 62.20.Mk

I. INTRODUCTION

The theory of quasistatic fractures in brittle media [1–5] calls for solving different equations depending on the mode of fracture. In this paper we present an approach based on iterated conformal maps which can be adapted to solve all three modes of fracture (known as modes I, II, and III), including the effects of inhomogeneities and randomness of the brittle material itself.

Basically, the theory of fracture in brittle continuous media is based on the equation of motion for an isotropic elastic body in the continuum limit [1]

$$\rho \frac{\partial^2 \mathbf{u}}{dt^2} = (\lambda+\mu)\boldsymbol{\nabla}(\boldsymbol{\nabla}\cdot\mathbf{u}) + \mu\nabla^2\mathbf{u}. \qquad (1)$$

Here **u** is the field describing the displacement of each mass point from its location in an unstrained body and ρ is the density. The constants μ and λ are the Lamé constants. In terms of the displacement field the elastic strain tensor is defined as

$$\epsilon_{ij} \equiv \frac{1}{2}\left(\frac{\partial u_i}{\partial x_j} + \frac{\partial u_j}{\partial x_i}\right). \qquad (2)$$

For the development of a crack the important object is the stress tensor, which in linear elasticity is written as

$$\sigma_{ij} \equiv \lambda\,\delta_{ij}\sum_k \epsilon_{kk} + 2\mu\epsilon_{ij}. \qquad (3)$$

When the stress component which is tangential to the interface of a crack exceeds a threshold value σ_c, the crack can develop. When the external load is such that the tangential stress exceeds only slightly the threshold value, the crack develops slowly, and one can neglect the second time derivative in Eq. (1). This is the quasistatic limit, in which after each growth event one needs to recalculate the strain field by solving the Lamé equation

$$(\lambda+\mu)\boldsymbol{\nabla}(\boldsymbol{\nabla}\cdot\mathbf{u}) + \mu\nabla^2\mathbf{u} = 0. \qquad (4)$$

The three "pure" modes of fracture that can be considered are determined by the boundary conditions, or load, at infinity. These are

$$\sigma_{xx}(\infty)=0; \quad \sigma_{yy}(\infty)=\sigma_\infty; \quad \sigma_{xy}(\infty)=0 \quad \text{(mode I)}, \qquad (5)$$

$$\sigma_{xx}(\infty)=0; \quad \sigma_{yy}(\infty)=0; \quad \sigma_{xy}(\infty)=\sigma_\infty \quad \text{(mode II)}. \qquad (6)$$

We will study the fracture patterns of these two modes in two-dimensional materials. Mode III calls for a third dimension z, since

$$\sigma_{zy}(y\rightarrow\pm\infty)=\sigma_\infty \quad \text{(mode III)}. \qquad (7)$$

Such an applied stress creates a displacement field $u_z(x,y)$, $u_x=0$, $u_y=0$ in the medium. Thus, in spite of the third dimension, the calculation of the strain and stress tensors remain two dimensional. Nevertheless, the equations to be solved in mode III and modes I and II are different. In mode III fracture $\boldsymbol{\nabla}\cdot\mathbf{u}=0$, and the Lamé equation reduces to Laplace's equation

$$\Delta u_z \equiv \partial^2 u_z/\partial x^2 + \partial^2 u_z/\partial y^2 = 0, \qquad (8)$$

and therefore u_z is the real part, Re $\chi(z)$, of an analytic function $\chi(z)$,

$$\chi(z) = u_z(x,y) + i\xi_z(x,y), \qquad (9)$$

where $z=x+iy$. The boundary conditions far from the crack and on the crack interface can be used to find this analytic function. On the other hand, for mode I and mode II fractures in plane elasticity one introduces [1] the Airy potential $U(x,y)$ such that

---

*Present address: Department Fisica, Facultad de Ciencias Fisicas y Matematicas, Universidad de Chile, Casilla 487-3, Santiago, Chile.

$$\sigma_{xx}=\frac{\partial^2 U}{\partial y^2}; \quad \sigma_{xy}=-\frac{\partial^2 U}{\partial x \partial y}; \quad \sigma_{yy}=\frac{\partial^2 U}{\partial x^2}. \tag{10}$$

The Airy potential U solves the bi-Laplacian equation [2]

$$\Delta\Delta U(x,y)=0. \tag{11}$$

The solution of the bi-Laplacian equation can be written in terms of *two* analytic functions $\phi(z)$ and $\eta(z)$ as

$$U(x,y)=\mathrm{Re}[\overline{z}\varphi(z)+\eta(z)]. \tag{12}$$

This difference requires therefore a separate discussion of mode III and modes I and II.

The problem of quasistatic crack propagation is difficult not only because it is hard to solve Eq. (4) for an arbitrarily shaped crack. Another source of difficulty is that the equation does not dictate how to propagate a crack when the stress tensor exceeds the threshold value σ_c. In this paper we consider only two-dimensional, or effectively two-dimensional (i.e, thin slabs) brittle materials in x,y. We can then describe a crack of arbitrary shape by its interface $\vec{x}(s)$, where s is the arc length which is used to parametrize the contour. We will use the notation (t,n) to describe, respectively, the tangential and normal directions at any point on the two-dimensional crack interface. The literature is quite in agreement that the velocity of propagation of the crack has a normal component which is some function of $\sigma_{tt}(s)-\sigma_c$ for mode I and II, and of $|\sigma_{zt}(s)|-\sigma_c$ for mode III. In both cases σ_c is a measure of the strength of the material, and fracture occurs only if the local stress tensor at the boundary of the crack exceeds this quantity (which can also be a random function of position). Although it is plausible that the normal velocity will depend on the excess stress, there is no proof that this is indeed so. Moreover, there is hardly a consensus on what that function the excess stress might be. The simplest choice [6,7] is a linear function,

$$v_n(s)=\alpha\Delta\sigma\equiv\alpha(\sigma_{tt}(s)-\sigma_c(s)), \quad \text{(modes I, II)}, \tag{13}$$

$$v_n(s)=\alpha\Delta\sigma\equiv\alpha(|\sigma_{zt}(s)|-\sigma_c(s)), \quad \text{(mode III)}, \tag{14}$$

when $\Delta\sigma\geqslant 0$, and $v_n(s)=0$ otherwise. Other velocity laws are possible [9]. In our study of mode III fracture we will examine also a quadratic and an exponential velocity law

$$v_n(s)=\alpha(|\sigma_{zt}(s)|-\sigma_c(s))^2 \quad \text{(mode III)}, \tag{15}$$

$$v_n(s)=e^{\alpha(|\sigma_{zt}(s)|-\sigma_c(s))} \quad \text{(mode III)}. \tag{16}$$

It is important to study these variants of the velocity law to ascertain the degree of universality of the geometric characteristics of the resulting cracks. One of our results is that these characteristics *may depend* on the velocity law. While this may be a disappointment from the point of view of fundamental physics, it may help to identify the correct physical mechanisms of fractures in different media. The lack of universality is even more obvious when we add quenched noise, or random values of $\sigma_c(s)$. The geometric characteristics of the cracks may depend on the probability distribution of random values of $\sigma_c(s)$. Again this may give a handle on the characterization of inhomogeneous brittle materials.

At any point in time there can be more than one position s on the interface for which $v_n(s)$ does not vanish. We choose the next growth position randomly with a probability proportional to $v_n(s)$ [7,8]. There we extend the crack by a fixed area of the size of the "process zone" (and see below for details). This is similar to diffusion limited aggregation (DLA) in which a particle is grown with a probability proportional to the gradient of the field. One should note that another model could be derived in which all eligible fracture sites are grown simultaneously, growing a whole layer whose local width is $v_n(s)$. This would be more akin to Laplacian growth algorithms, which in general give rise to clusters in a different universality class than DLA [10,11].

In Sec. II we discuss the growth algorithm in terms of iterated conformal maps. In Sec. III this method is applied to mode III quasistatic fracture. A preliminary report of the method for this case was presented in Ref. [12]. In Sec. IV we present new results including the consequences of the different velocity laws (15) and (16), and those of quenched randomness. We discuss the geometric properties of the fracture patterns, including issues of roughening and exponents. We point out that the roughening exponents are not always well defined, since the fracture patterns do not have stationary geometric characteristics. There is an increased tendency for ramification as the fracture develops. This is reflected in an apparent increase in the roughening exponents of the backbone of the pattern. In Sec. V we discuss the theory of modes I and II fracture. Sec. VI presents the results. We will see that the fracture patterns in modes I and II are much less rough than in mode III (for the same velocity law), in agreement with the analysis of Ref. [13]. We will conclude the paper in Sec. VII. The main conclusion is that mode III results in cracks whose geometric characteristics are in a different class than modes I and II. The former creates cracks that exhibit a cross over in the averaged roughening exponent from about 0.5 to a higher scaling exponent on the larger scales. In contrast, modes I and II create cracks that are not rough on the large scales. Quenched randomness may affect the geometry of the cracks as is exemplified and discussed in this paper.

II. THE METHOD OF ITERATED CONFORMAL MAPS FOR FRACTURE

The direct determination of the strain tensor for an arbitrary shaped (and evolving) crack is difficult. We therefore proceed by turning to a mathematical complex plane ω, in which the crack is forever circular and of unit radius. Next invoke a conformal map $z=\Phi^{(n)}(\omega)$ that maps the exterior of the unit circle in the mathematical plane ω to the exterior of the crack in the physical plane z, after n growth steps. The conformal map will be univalent by construction, and we can write its Laurent expansion in the form

$$\Phi^{(n)}(\omega)=F_1^{(n)}\omega+F_0^{(n)}+F_{-1}^{(n)}/\omega+F_{-2}^{(n)}/\omega^2+\cdots. \tag{17}$$

For all modes of fracture we take $\Phi^{(0)}(\omega)=\omega$, and the iterative dynamics calls for the calculation of the tangential component of the stress tensor on the boundary of the crack. The arclength position s in the physical domain is mapped by the inverse of $\Phi^{(n)}$ onto a position on the unit circle $\omega = \exp(i\theta)$. We will be able to compute the stress tensor on the boundary of the crack in the physical domain by performing the calculation on the unit circle. In other words we will compute $\sigma_{tt}(\theta)$ or $\sigma_{zt}(\theta)$ on the unit circle in the mathematical plane. The actual calculation of this component of the stress tensor differs in modes I, II, and mode III. We perform the calculation iteratively, taking the stress as known for the crack after $n-1$ fracture events.

In order to implement the nth cracking event according to one of the required velocity laws (13)–(16), we should choose potential positions on the interface more often when v_n is larger. Consider for example the linear velocity law (13). We construct a probability density $P(\theta)$ on the unit circle $e^{i\theta}$ which satisfies

$$P(\theta)=\frac{|\Phi'^{(n-1)}(e^{i\theta})|\Delta\sigma(\theta)\Theta(\Delta\sigma(\theta))}{\int_0^{2\pi}|\Phi'^{(n-1)}(e^{i\tilde{\theta}})|\Delta\sigma(\tilde{\theta})\Theta(\Delta\sigma(\tilde{\theta}))d\tilde{\theta}}, \quad (18)$$

where $\Theta(\Delta\sigma(\tilde{\theta}))$ is the Heaviside function, and $|\Phi'^{(n-1)}(e^{i\theta})|$ is simply the Jacobian of the transformation from mathematical to physical plane. The next growth position, θ_n in the mathematical plane, is chosen randomly with respect to the probability $P(\theta)d\theta$. At the chosen position on the crack, i.e. $z=\Phi^{(n-1)}(e^{i\theta_n})$, we want to advance the crack with a region whose area is the typical process zone for the material that we analyze. According to Ref. [3] the typical scale of the process zone is K^2/σ_c^2, where K is a characteristic fracture toughness parameter. Denoting the typical *area* of the process zone by λ_0, we achieve growth with an auxiliary conformal map $\phi_{\lambda_n,\theta_n}(\omega)$ that maps the unit circle to a unit circle with a bump of area λ_n centered at $e^{i\theta_n}$. An example of such a map is given by [14,15]

$$\phi_{\lambda,0}(w)=w^{1-a}\left\{\frac{(1+\lambda)}{2w}(1+w)\times\left[1+w+w\left(1+\frac{1}{w^2}-\frac{2}{w}\,\frac{1-\lambda}{1+\lambda}\right)^{1/2}\right]-1\right\}^{a} \quad (19)$$

$$\phi_{\lambda,\theta}(w)=e^{i\theta}\phi_{\lambda,0}(e^{-i\theta}w). \quad (20)$$

Here the bump has an aspect ratio a, $0\leqslant a\leqslant 1$. In our work below we use $a=1/2$. To ensure a fixed size step in the physical domain we choose

$$\lambda_n=\frac{\lambda_0}{|\Phi^{(n-1)\prime}(e^{i\theta_n})|^2}. \quad (21)$$

Finally the updated conformal map $\Phi^{(n)}$ is obtained as

$$\Phi^{(n)}(\omega)=\Phi^{(n-1)}(\phi_{\lambda_n,\theta_n}(\omega)). \quad (22)$$

The recursive dynamics can be represented as iterations of the map $\phi_{\lambda_n,\theta_n}(w)$,

$$\Phi^{(n)}(w)=\phi_{\lambda_1,\theta_1}\circ\phi_{\lambda_2,\theta_2}\circ\dots\circ\phi_{\lambda_n,\theta_n}(\omega). \quad (23)$$

Every given fracture pattern is determined completely by the random itinerary $\{\theta_i\}_{i=1}^{n}$.

We should stress at this point that this method of development of the fracture pattern is not purely based on linear elasticity. Every growth step advances the fractured zone over an area of the order of λ_0. This represents events that occur in the "process zone," in which plastic flows are taking place, and which are not within the realm of elasticity theory, linear or not. We also note that the fracture patterns shown below are the results of this iterated growth process, and the stress field is computed again after each growth step. The deformation due to the stress field is not represented in the patterns, being an effect of second order.

III. MODE III QUASISTATIC FRACTURE

In this section we discuss how to compute the stress tensor when the load is mode III, using the method of iterated conformal maps. The first step is the determination of the boundary conditions that the analytic function (9) needs to satisfy.

A. Boundary conditions in mode III

Far from the crack as $y\to\pm\infty$ we know $\sigma_{zy}\to\sigma_\infty$ or using the stress-strain relationships Eq. (3) we find that $u_z \approx [\sigma_\infty/\mu]y$. Thus the analytic function must have the form

$$\chi(z)\to -i[\sigma_\infty/\mu]z \quad \text{as } |z|\to\infty. \quad (24)$$

Now on the boundary of the crack the normal stress vanishes, i.e.,

$$0=\sigma_{zn}(s)=\partial_n u_z=-\partial_t \xi_z. \quad (25)$$

This means that ξ_z is constant on the boundary. We choose the gauge $\xi_z=0$, which in turn is a boundary condition making the analytic function $\chi(z)$ real on the boundary of the crack,

$$\chi(z(s))=\chi(z(s))^*. \quad (26)$$

B. The stress tensor for mode III

Following the basic strategy we consider now a circular crack in the mathematical domain. The strain field for such a crack is well known [2], being the real part of the function $\chi^{(0)}(\omega)$ where

$$\chi^{(0)}(\omega)=-i[\sigma_\infty/\mu](\omega-1/\omega). \quad (27)$$

This is the unique analytic function obeying the boundary conditions $\chi^{(0)}(\omega)\to -i[\sigma_\infty/\mu]\omega$ as $|\omega|\to\infty$, while on the unit circle $\chi^{(0)}(\exp(i\theta))=\chi^{(0)}(\exp(i\theta))^*$. To find the corresponding function in the physical plane is particularly easy for mode III. Since the real part of the function $\chi(z)$ is

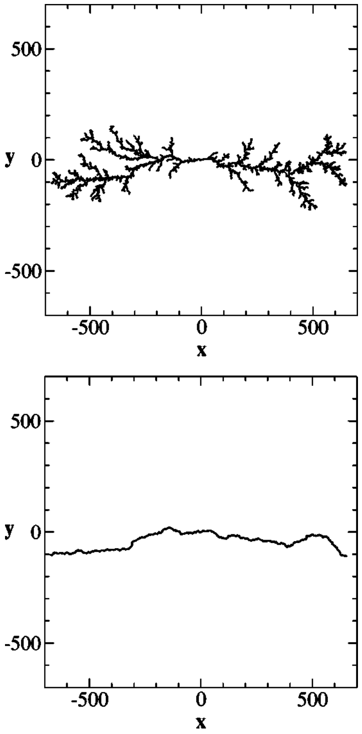

FIG. 1. Upper panel: a typical mode III fracture pattern that is obtained from iterated conformal maps. What is seen is the boundary of the fractured zone, which is the mapping of the unit circle in the mathematical domain onto the physical domain. Notice that the pattern becomes more and more ramified as the the fracture pattern develops. This is due to the enhancement of the stress field at the tips of the growing pattern. Lower panel: the backbone of the fracture pattern. This is the projection onto the *x*-*y* plane of the experimentally observed boundary between the two parts of the material that separate when the fracture pattern hits the lateral boundaries.

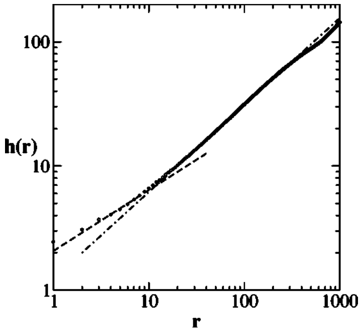

FIG. 2. $h(r)$ averaged over all the backbone and over 20 fracture patterns each of which of 10 000 fracture events. There is a crossover between a scaling law with roughness exponent 0.49 ± 0.08 to an exponent of 0.70 ± 0.05.

analytic, it satisfied Laplace's equation automatically. We only need to make sure that it satisfies the boundary conditions. However, if we have a good solution in the mathematical plane, we need just to compose it with an analytic function that takes us from the physical to the mathematical plane. The required analytic function $\chi^{(n)}(z)$ is given by the expression

$$\chi^{(n)}(z)=-i[F_1^{(n)}\sigma_\infty/\mu][\Phi^{(n)-1}(z)-1/\Phi^{(n)-1}(z)]. \tag{28}$$

(If $\Phi^{(n)}$ is conformal, $\Phi^{(n)-1}$ is analytic by definition). From this we should compute now the tangential stress tensor,

$$\begin{aligned}\sigma_{zt}(s)&=\mu\partial_t u_z=\mu\,\mathrm{Re}\left[\frac{\partial\chi^{(n)}(z)}{\partial s}\right]\\&=\mu\,\mathrm{Re}\left[\frac{\partial\chi^{(n)}(\Phi^{(n)}(e^{i\theta}))}{\partial\theta}\frac{\partial\theta}{\partial s}\right]\\&=-\mathrm{Re}\frac{iF_1^{(n)}\sigma_\infty\frac{\partial}{\partial\theta}(e^{i\theta}-e^{-i\theta})}{|\Phi'^{(n)}(e^{i\theta})|}\\&=2\sigma_\infty F_1^{(n)}\frac{\cos\theta}{|\Phi'^{(n)}(e^{i\theta})|},\end{aligned}\tag{29}$$

on the boundary. Eqs. (29) together with Eq. (23) offer an analytic expression for the tangential stress field at any stage of the crack propagation.

IV. RESULTS FOR MODE III

A. Linear velocity law

Figure 1 exhibits in the upper panel a typical fracture pattern that is obtained with this theory, with $\sigma_\infty=1$, after 10 000 growth events. The threshold value of σ_c for the occurrence of the first event [cf. Eq. (29)] is $\sigma_c=2$. We always implement the first event. For the next growth event the threshold of σ_c is $2.34315\cdots$. We thus display in Fig. 1 a cluster obtained with $\sigma_c=2.00$, to be close to the quasistatic limit. Note that here we could opt to represent a disordered material by a random value of σ_c, and see Sec. IV C. With fixed σ_c, one should observe that as the pattern develops, the stress at the active zone increases, and we get progressively away from the quasistatic limit. One could perform a different calculation, relaxing the stress at infinity such as to keep the growth close to threshold. But with fixed boundary conditions at infinity, there are more and more values of θ for which Eq. (18) does not prohibit growth. Since the tips of the patterns are mapped by $\Phi^{(n)-1}$ to larger and larger arcs on the unit circle, the support of the probability $P(\theta)$ increases, and the fracture pattern becomes more and more ramified as the process advances. The geometric characteristics of the fracture pattern are *not* invariant to the growth. For this reason it makes little sense to measure the fractal dimension of the pattern; this is not a stable characteristic, and it will change with the growth. On the other hand, we should realize that the fracture pattern is not what is observed in typical experiments. When the fracture hits the boundaries of the sample, and the sample breaks into two parts, all the side-branches of the pattern remain hidden in the damaged material, and only the backbone of the fracture pattern appears as the surface of the broken parts. In the lower panel of Fig. 1 we show the backbone of the pattern displayed in the upper panel.

This backbone is the representative of all the fracture patterns with the linear velocity law. We should note that in our theory there are no lateral boundaries, and the backbone shown does not suffer from finite size effects which may very well exist in experimental realizations.

In determining the roughness exponent of the backbone, we should note that a close examination of it reveals that *it is not a graph*. There are overhangs in this backbone, and since we deal with mode III fracturing, the two pieces of material *can* separate leaving these overhangs intact. Accordingly, one should not approach the roughness exponent using correlation function techniques; these may introduce serious errors when overhangs exist [16]. Rather, we should measure, for any given r, the quantity [17]

$$h(r) \equiv \langle \max\{y(r')\}_{x<r'<x+r} - \min\{y(r'\}_{x<r'<x+r} \rangle_x . \tag{30}$$

The roughness exponent ζ is then obtained from

$$h(r) \sim r^{\zeta}, \tag{31}$$

if this relation holds. To get good statistics we average, in addition to all x for the same backbone, over many fracture patterns. The result of the analysis is shown in Fig. 2.

We find that the roughness exponent for the backbone exhibits a clear crossover from about 0.5 for shorter distances r to about 0.70 for larger distances. Within the error bars these results are in a surprising agreement with the numbers quoted experimentally, see for example, Ref. [17]. The short length scale exponent of order 0.5 is also in agreement with recent simulational results of a lattice model [18] (which is by definition a short length scale solution). Bouchaud [17] proposed that the crossover stems from transition between slow and rapid fracture, from the "vicinity of the depinning transition" to the "moving phase" in her terms. Obviously, in our theory we solve the quasistatic equation all along, and there is no change of physics. In addition, there is no reason to expect the experiment to be a pure mode III, and as we will see below modes I and II do not show similar roughening. Nevertheless, as we observed before, the fracture pattern begins with very low ramification when the stress field exceeds the threshold value only at few positions on the fracture interface. Later it evolves to a much more ramified pattern due to the increase of the stress fields

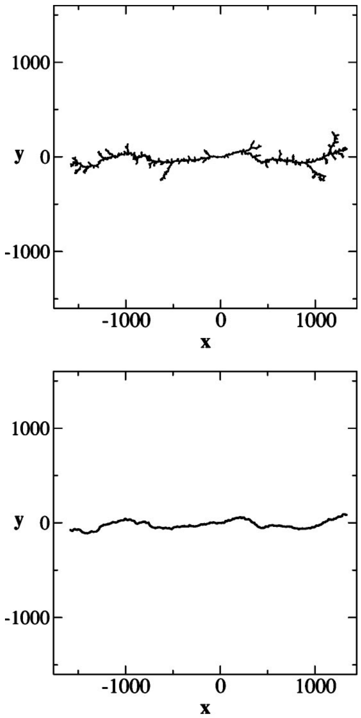

FIG. 3. Upper panel: fracture pattern for mode III fracture with the quadratic law (15), with 10 000 fracture events. Lower panel: the backbone of the pattern.

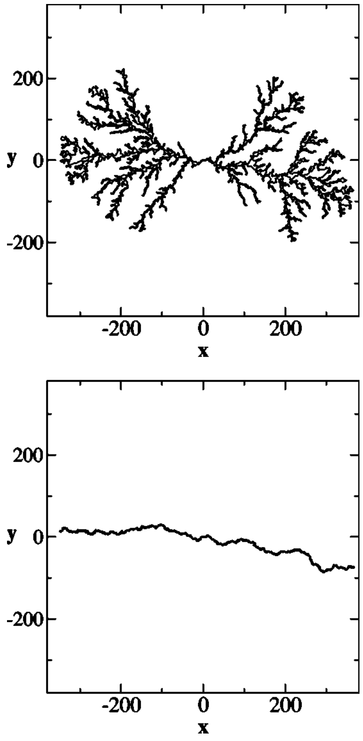

FIG. 4. Upper panel: fracture pattern for mode III fracture with the exponential law (16), with $\alpha=0.1$, with 10 000 fracture events. Lower panel: the backbone of the pattern.

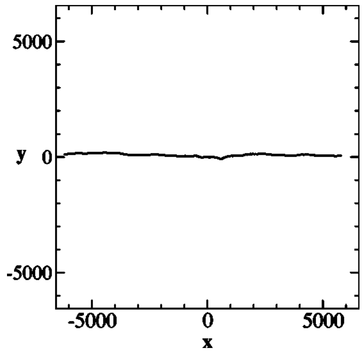

FIG. 5. Fracture pattern for mode III fracture with the exponential law (16), with $\alpha=1$, with 10 000 fracture events. In this case the fracture pattern and the backbone are the same.

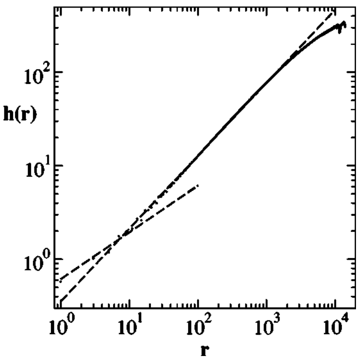

FIG. 6. $h(r)$ averaged over 20 fracture patterns with the exponential velocity law with $\alpha=1$. Each of the patterns consists of 10 000 fracture events. There is a cross over between a scaling law with roughness exponent of about 0.50 at short length scales to an apparent scaling exponent of about 0.78.

at the tips of the mature pattern. *The scaling properties of the backbone reflect this crossover*. We propose that this effect is responsible for the crossover in the roughening exponent of the backbone. On the other hand, this nonstationarity in the geometric characteristics should be handled with care, since it may mean that there is no definite roughening exponent, as it may depend on *where* the analysis is done, near the center of the fracture patterns or near the edge. We will return to this delicate issue after reviewing the results of other velocity laws.

B. Other velocity laws

It should be stressed that there is no reason to believe that the scaling exponents are invariant to the change of the velocity law. In Figs. 3, 4, and 5 we show the fracture patterns and their corresponding backbones for the quadratic velocity law (15) and for two different exponential laws (16). We find that the quadratic law makes little difference with respect to the linear law. The roughening plot is similar, and the scaling exponents appear the same. The exponential velocity law changes the degree of ramification, and therefore calls for a careful discussion of the roughening plots. Examine the function $h(r)$ for the pattern in Fig. (5) (see Fig. 6). While the small scale roughening exponent of about 0.5 is reproduced, it appears that the large scale exponent is now higher, about 0.78. The question to be asked therefore is whether the scaling exponent is not invariant to the velocity law. In our opinion this question is ill posed since the scaling exponent itself *depends on where is it measured*. As we said before, the fracture pattern tends to become more ramified as it grows. This is reflected in the roughening properties. To make this point clearer, we have taken the pattern of Fig. 5 as a test case, and computed the apparent scaling exponents for short parts of the fracture pattern, limiting the maximal value of r to 2000. By doing so, we can concentrate on a region near the center of the pattern, and on a region near the edge. The results of this exercise are presented in Fig. 7 What is found is that the apparent scaling exponent depends on the region of measurements. Near the center, where the pattern is less ramified, the exponent is smaller than near the edge where the pattern is more ramified. The average exponent reported in Fig. 6 which is analogous to what is reported in experiments, has therefore a limited value. It may not be interpreted as a ‘‘true’’ scaling exponents. Its value may well depend on the actual length of the pattern that is investigated.

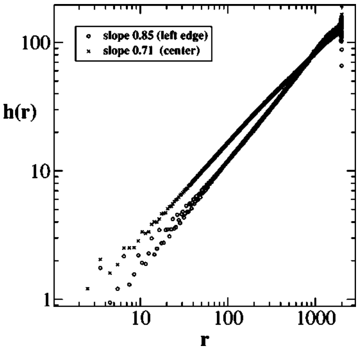

FIG. 7. $h(r)$ averaged over 20 fracture patterns with the exponential velocity law with $\alpha=1$. In this calculation we concentrate on parts of the pattern shown in Fig. 5, one near the center and the other near the edge, each consisting of $r=2000$. The apparent exponents differ, being 0.71 at the center and 0.85 near the edge. The average behavior with exponent 0.78 seen in Fig. 6 should therefore be interpreted with extra care.

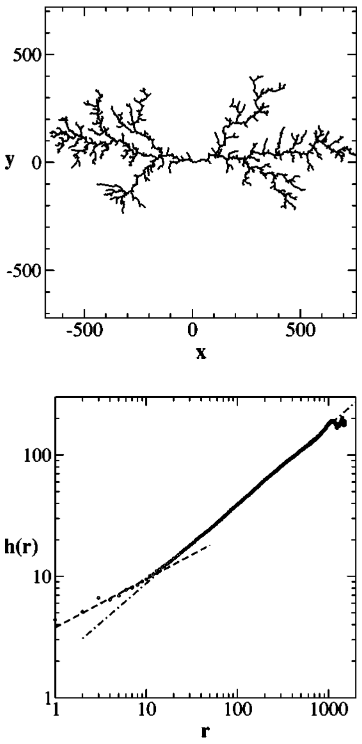

FIG. 8. Upper panel: fracture pattern for mode III fracture with the linear velocity law and quenched randomness with a flat distribution, $\sigma_{max}=15$, with 10 000 fracture events. Lower panel: the function $h(r)$ after averaging over 20 patterns. The scaling exponents are about 0.4 and 0.65 for the smaller and larger scales, respectively.

We are therefore not in a position to claim that the correspondence in roughening exponents between the linear law and experiments indicates anything about universality

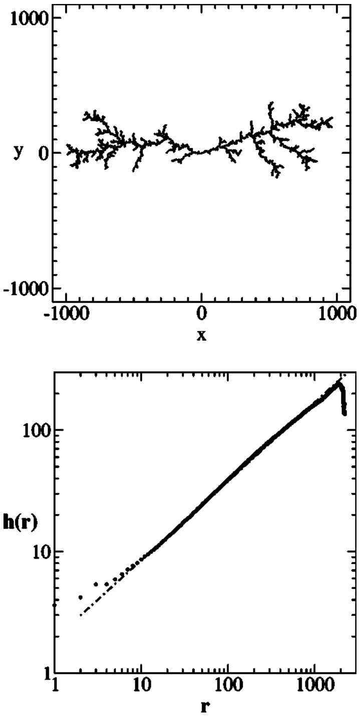

FIG. 9. Upper panel: Fracture pattern for mode III fracture with the linear velocity law and quenched randomness with a power-law distribution, $\beta=2,\sigma_{min}=2$, with 10 000 fracture events. Lower panel: the function $h(r)$ after averaging over 20 patterns. The scaling exponent is about 0.65.

classes. One needs to ascertain very carefully whether measured roughening exponents indicate translationally invariant scaling properties. It is in particular useful to know whether the observed scaling exponents depends on the length of the available fracture pattern.

C. Quenched disorder

To study the effect of quenched randomness we assign *a priori* a random value σ_c to every point in the material (with resolution λ_0). Not having a clear indication from the literature how the randomness of inhomogeneous media should be modeled, we opted for two types of quenched randomness. The first takes the numerical value of $\sigma_c(s)$ from a flat distribution, $0\leqslant\sigma_c\leqslant\sigma_{max}$ and the second takes a power-law form

$$P(\sigma_c)\propto\sigma_c^{-\beta} \quad \text{for} \quad \sigma_c>\sigma_{min}. \tag{32}$$

For reasonable values of σ_{max} the flat distribution did not lead to a qualitative change in the fracture patterns. In Fig. 8 we show the pattern and the function $h(r)$ for the case $\sigma_{max}=15$. The typical crossover that we see in systems without quenched disorder remains here, albeit with apparently smaller exponents, of about 0.4 and 0.65.

On the other hand, a power-law distribution of quenched randomness may lead to very interesting qualitative change in fracture pattern. While high values of β in Eq. (32) are still in qualitative agreement with all previous results (see Fig. 9 with $\beta=2$), lower values of β lead to a new phenomenon. The availability of very high values of σ_c results in effective blocking for the evolution of the fracture. The crack develops along continuous (sometime curved) lines, and then it suddenly gains sharp turns. In Fig. 10 we show the typical patterns obtained for $\beta=1.1$. It is amusing to note that these patterns are reminiscent of what is exhibited in a number of experiments and see, for example, the pictures in Ref. [17]. It is not obvious, however, how to offer quantitative measures for comparison. It appears to the present authors that this subject of fracture with quenched randomness deserves a careful separate study in which experimental and theoretical methods were combined to gain further insights on the questions at hand.

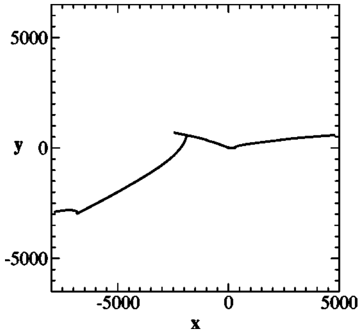

FIG. 10. Fracture pattern for mode III fracture with the linear velocity law and quenched randomness with a power-law distribution, $\beta=1.1,\sigma_{min}=0.2$.

V. THEORY FOR MODES I AND II

In order to compute the stress tensor at the boundary of the crack for modes I and II loading, we turn to the solution of Eq. (11). Since we employ conformal techniques, we are limited to solving Eq. (11) in two-dimensions. Although we realize that three-dimensional solutions may introduce additional physics and quantitative changes [13], we trust that a controlled solutions of Eq. (11) in two-dimensions will shed useful light on the questions of crack geometry, roughening, and scaling.

A. Boundary conditions and removal of freedoms

The boundary conditions at infinity are given by Eqs. (5) and (6). The conditions on the boundary of the crack are

$$\sigma_{xn}(s)=\sigma_{yn}(s)=0 \quad \text{on the boundary.} \tag{33}$$

Using Eq. (10) these boundary condition are rewritten as

$$\partial_t\left[\frac{\partial U}{\partial x}+i\frac{\partial U}{\partial y}\right]=0 \quad \text{on the boundary.} \tag{34}$$

Note that we do not have enough boundary conditions to determine $U(x,y)$ uniquely. In fact we can allow in Eq. (12) arbitrary transformations of the form

$$\varphi\rightarrow\varphi+iCz+\gamma, \tag{35}$$

$$\psi \rightarrow \psi + \tilde{\gamma}, \quad \psi \equiv \eta', \tag{36}$$

where C is a real constant and γ and $\tilde{\gamma}$ are complex constants. This provides five degrees of freedom in the definition of the Airy potential. Two of these freedoms are removed by choosing the gauge in Eq. (34) according to

$$\frac{\partial U}{\partial x} + i\frac{\partial U}{\partial y} = 0 \quad \text{on the boundary.} \tag{37}$$

It is important to stress that whatever the choice of the five freedoms the values of the stress tensor are unaffected, and see Ref. [2] for an exhaustive discussion of this point. Computing Eq. (37) in terms of Eq. (12) we arrive at the boundary condition

$$\varphi(z) + z\overline{\varphi'(z)} + \overline{\psi(z)} = 0 \quad \text{on the boundary.} \tag{38}$$

To proceed we represent $\varphi(z)$ and $\psi(z)$ in Laurent form.

$$\varphi(z) = \varphi_1 z + \varphi_0 + \varphi_{-1}/z + \varphi_{-2}/z^2 + \cdots,$$

$$\psi(z) = \psi_1 z + \psi_0 + \psi_{-1}/z + \psi_{-2}/z^2 + \cdots. \tag{39}$$

This form is in agreement with the boundary conditions at infinity that disallow higher-order terms in z. The remaining freedoms are now used to choose $\varphi_0 = 0$ and φ_1 real. Then, using the boundary conditions (5) and (6), we find

$$\varphi_1 = \frac{\sigma_\infty}{4}; \quad \psi_1 = \frac{\sigma_\infty}{2} \quad \text{mode I},$$

$$\varphi_1 = 0; \quad \psi_1 = i\sigma_\infty \quad \text{mode II}. \tag{40}$$

B. The conformal map and its consequences

The conformal map is identical in form and meaning to the one introduced above and successfully applied to mode III. On the other hand, at present we do not solve the Laplace equation, and our fundamental solution (12) is *not* the real part of an analytic function. We thus cannot simply solve in the mathematical plane and compose with the inverse of the conformal map.

In terms of the conformal map we will write our unknown functions $\varphi(z)$ and $\psi(z)$ as

$$\varphi(z) \equiv \tilde{\varphi}(\Phi^{(n)-1}(z)), \quad \psi(z) \equiv \tilde{\psi}(\Phi^{(n)-1}(z)). \tag{41}$$

Using the Laurent form (17) of the conformal map the linear term at $\omega \rightarrow \infty$ is determined by Eqs. (41). We therefore can write

$$\tilde{\varphi}(\omega) = \varphi_1 F_1^{(n)}\omega + \tilde{\varphi}_{-1}/\omega + \tilde{\varphi}_{-2}/\omega^2 + \cdots,$$

$$\tilde{\psi}(\omega) = \psi_1 F_1^{(n)}\omega + \tilde{\psi}_0 + \tilde{\psi}_{-1}/\omega + \tilde{\psi}_{-2}/\omega^2 + \cdots. \tag{42}$$

The boundary condition (38) is now read for the unit circle in the ω plane. Denoting $\epsilon \equiv \exp(i\theta)$ and

$$u(\epsilon) \equiv \sum_{n=1}^{\infty} \tilde{\varphi}_{-n}/\epsilon^n, \quad v(\epsilon) \equiv \sum_{n=0}^{\infty} \tilde{\psi}_{-n}/\epsilon^n, \tag{43}$$

we write

$$u(\epsilon) + \frac{\Phi^{(n)}(\epsilon)}{\overline{\Phi'^{(n)}(\epsilon)}}\overline{u'(\epsilon)} + \overline{v(\epsilon)} = f(\epsilon). \tag{44}$$

The function f is a known function that contains all the coefficients that were determined so far,

$$f(\epsilon) = -\varphi_1 F_1^{(n)}\epsilon - \frac{\Phi^{(n)}(\epsilon)}{\overline{\Phi'^{(n)}(\epsilon)}}\varphi_1 F_1^{(n)} - \frac{\overline{\psi_1} F_1^{(n)}}{\epsilon}. \tag{45}$$

C. Solution by power series

To solve the problem we need to compute the coefficients $\tilde{\varphi}_n$ and $\tilde{\psi}_n$. To this aim we first represent

$$\frac{\Phi^{(n)}(\epsilon)}{\overline{\Phi'^{(n)}(\epsilon)}} = \sum_{-\infty}^{\infty} b_i \epsilon^i. \tag{46}$$

The function $f(\sigma)$ has also an expansion of the form

$$f(\epsilon) = \sum_{-\infty}^{\infty} f_i \epsilon^i. \tag{47}$$

In the discussion below we assume that the coefficients b_i and f_i are known. In fact what is computed in our procedure is the conformal map $\Phi^{(n)}(\omega)$. Thus to compute these coefficients we need to Fourier transform the function $\Phi^{(n)}(\epsilon)/\overline{\Phi'^{(n)}(\epsilon)}$. This is the most expensive step in our solution, since the branch cuts that exist in Eq. (19) rule out the use of fast Fourier transforms. One needs to carefully evaluate the Fourier integrals between the branch cuts. The technique how to track the position of the branch cuts on the unit circle was developed in Refs. [10,11]; after having the branch cuts the integrals are evaluated over 1000 equi-distant points between each pair of branch cuts. Using the last two equations together with Eqs. (43) and (44) we get

$$\tilde{\varphi}_{-m} - \sum_{k=1}^{\infty} k\, b_{-m-k-1}\tilde{\varphi}^*_{-k} = f_{-m}, \quad m = 1,2,\ldots, \tag{48}$$

$$\tilde{\psi}^*_{-m} - \sum_{k=1}^{\infty} k\, b_{m-k-1}\tilde{\varphi}^*_{-k} = f_m, \quad m = 0,1,2,\ldots. \tag{49}$$

These sets of linear equations are well posed. The coefficients $\tilde{\varphi}_{-m}$ can be calculated from Eq. (48) alone, and then they can be used to determine the coefficients $\tilde{\psi}_{-m}$. This is in fact proof that Eq. (44) determines the functions u and v together. This fact had been proven with some generality in Ref. [2].

For cracks with simple geometry this is all that we need. For example for a circular crack (a problem that was explicitly solved in Ref. [2]) we simply substitute $\Phi^{(n)}(\omega) = \Phi^{(0)}(\omega) = \omega$, and proceed to solve for $\tilde{\varphi}$ and $\tilde{\psi}$, finding finally

$$\tilde{\varphi}(\omega) = \varphi_1 \omega - \frac{\psi_1^*}{\omega}, \quad \tilde{\psi}(\omega) = \psi_1 \omega - 2\frac{\varphi_1}{\omega} - \frac{\psi_1^*}{\omega^3}. \tag{50}$$

For developing cracks of arbitrary shape this is just the starting point. As before in the solution of mode III we need to compute σ_{tt} from which we construct the probability measure for the first fracture event. The development of the $\Phi^{(n)}$ then follows the same lines as before.

To compute σ_{tt} at the boundary of the crack we use the fact that follows directly from the definitions that

$$\sigma_{xx} + \sigma_{yy} = 4\,\mathrm{Re}[\varphi'(z)] = 4\,\mathrm{Re}\left[\frac{\tilde{\varphi}'(\omega)}{\Phi'^{(n)}(\omega)}\right]. \tag{51}$$

Since this is the trace of the stress tensor, which is invariant under smooth coordinate transformation, it is also equal to $\sigma_{nn} + \sigma_{tt}$. Using the fact that σ_{nn} vanishes on the boundary we can write finally

$$\sigma_{tt}(\epsilon) = 4\,\mathrm{Re}\left[\frac{\tilde{\varphi}'(\epsilon)}{\Phi'^{(n)}(\epsilon)}\right]. \tag{52}$$

This result is of some importance; it shows that to compute the component σ_{tt} of the stress tensor *on the boundary* we do not need to compute $\tilde{\psi}(\epsilon)$ at all. Of course, to know the stress tensor anywhere else in the body we need both functions. For the growth algorithm this is not necessary. We note that $\tilde{\varphi}$ is computed from Eqs. (48), and this contains only b_m with negative m. In order to derive a numerical scheme to compute the tangent stress component σ_{tt} on the crack we now truncate the series for $\tilde{\varphi}$ to get an approximation

$$u(\epsilon) \approx \sum_{n=1}^{N} \tilde{\varphi}_{-n}/\epsilon^n. \tag{53}$$

We see from Eq. (48) that if we wish to compute this series up to an order N, we need to compute the coefficients b_{-j} up to $j \leq 2N+1$ and then solve the linear system (48). Note that the approximation in Eq. (53) corresponds to a truncation of the series (46) which in turn corresponds to a truncation of the conformal map $\Phi^{(n)}$. Since we are interested in the macroscopic stress distribution along the fracture rather than in the bumpy microstructure, this effect is of no harm as long as we choose N large enough to resolve the desired patterns.

VI. RESULTS FOR MODES I AND II

A. Geometry without quenched disorder

The actual fracture patterns that we find for modes I and II are dramatically different from those found for mode III for the same velocity law. In Fig. 11 we show the fracture patterns for the linear velocity law after about 800 fracture events. First, modes I and II are very similar, except for the obvious 45° tilt in mode II due to the tilt of the symmetry axis of the loading. The highly ramified structure seen in mode III is gone, and the resulting patterns are more akin to the exponential velocity law in mode III, cf. Fig. 5. The roughening plot $h(r)$ (Fig. 12) is also qualitatively different from mode III with the same velocity law. We do not observe a crossover to a higher exponent, indicating that there is no increased roughening at large scales. Indeed, for these modes of fracture the stress field is found to be very highly peaked at the tip of the fracture pattern. Moreover, when there appear deviations towards side branching they are quickly corrected in later growth. To make this point clearer we present in Fig. 13 the stress field at the boundary of the crack in the vicinity of the tip. One can observe that the stress component is such that the slight tilt of the tip will be corrected at the

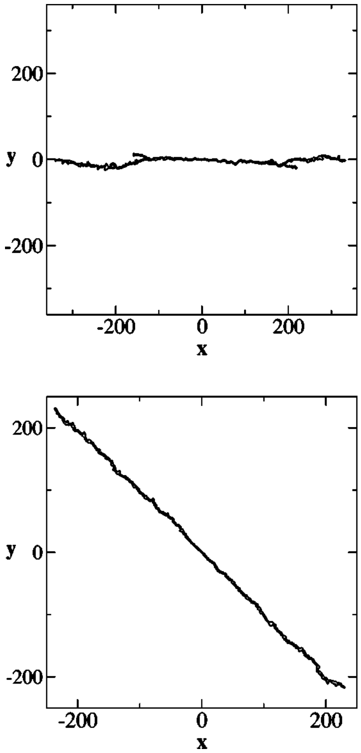

FIG. 11. Upper panel: fracture pattern for mode I with the linear velocity law. Lower panel: fracture pattern for mode II with the linear velocity law.

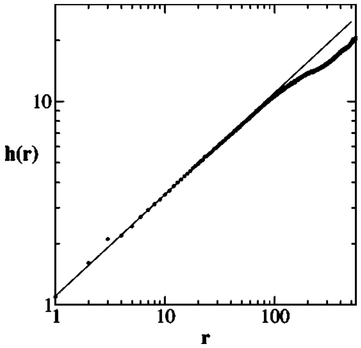

FIG. 12. The function $h(r)$ for mode I fracture, averaged over 11 fracture patterns. The line indicates a slope of 0.5.

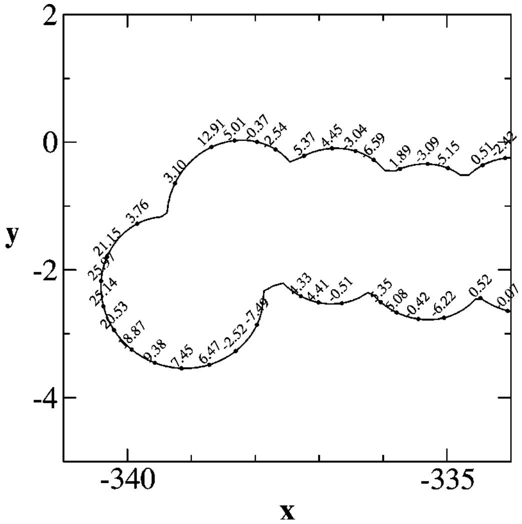

FIG. 13. The stress field at the boundary of the crack in the vicinity of the tip.

next growth event. We therefore do not expect large scale roughening in this mode of fracture.

We should note that similarity in the crack geometries in modes I and II stems from the fact that we distinguish these two modes only by boundary conditions at infinity. Without material anisotropy the crack of mode II chooses an orientation of 45°, rendering the local dynamics at the interface identical to mode I, except for the tilt. At present we do not see how to select boundary conditions that load the crack *locally* in mode II. This phenomenon is related to the so-called ''principle of local symmetry'' [19] that underlines the preference of cracks to maximize their mode I loading at the expense of mode II.

B. The effect of quenched disorder

Last, we present cracks with quenched disorder. First we followed the growth of a crack in mode I, using the same strategy of Sec. IV C. In Fig. 14 we show, for example, the crack obtained with σ_c taken from a flat distribution with $\sigma_{max}=10$. Contrary to the case of mode III the effect of quenched disorder on the roughening is not impressive. The roughening exponent is still about 0.5 for small scales, with a failure to roughen on the large scales. This finding remains invariant to change the type of quenched disorder to a power law like Eq. (32). We also do not observe roughening on the large scales when we put quenched disorder, and grow deterministically at the point of highest value of $\sigma_{tt}-\sigma_c$.

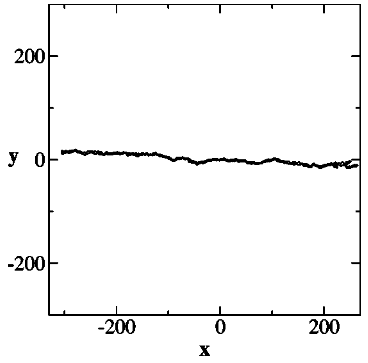

FIG. 14. The fracture pattern in the case of quenched disorder, with σ_c taken from a flat distribution. The pattern is similar to that in Fig. 11, with the same roughening behavior.

VII. CONCLUDING REMARKS

We have presented a solution of the problem quasistatic fracture using the method of iterated conformal map. All modes of fracture can be treated, although mode III is much more straightforward since the equation to be solved is the Laplace equation. The bi-Laplacian equation that is involved in modes I and II requires heavier analysis and more cumbersome numerics. Notwithstanding, we believe that our fracture patterns represent accurate solutions of the problem with the stated laws of evolution.

The geometric characteristics of mode III are different from those of modes I and II. The fracture pattern is very ramified, and if we look at the backbone, (which is what is observed as the boundary between the two parts of the broken material), we find that it is rough on all scales. On smaller scales the roughening exponent is about 0.5, and on larger scales the roughening increases, having an average roughening exponent which depends on the length of the fracture pattern analyzed. The exponent 0.5 is intimately related to the randomness that is introduced by our growth rules. the higher apparent exponents are due to the increased ramification on the larger scales as is explained in Sec. IV. The roughening plots may appear to be in close agreement with some experimental observations, which however are not conducted as mode III. Experimentally one expects that modes I and II are more relevant, but here we do not observe the crossover to roughness characterized by exponents of the order of 0.75. Quite on the opposite, it appears that the roughness saturates, leading to a globally flat fracture patterns on the large scales.

This leaves us with the question of how to interpret the observed roughness in experiments. One possibility is that experiments are not quasistatic, or that in experiments the material has remnant stresses and other sources of quenched disorder. This is the spirit for example of Ref. [20] (and references therein) in which the crossover is tentatively related to damage cavity coalescence. Such possibilities can be put to test. Indeed, we find that mode III is very sensitive to quenched disorder, cf. Sec. IV C. With power-law disorder we can change the geometric characteristic of the fracture patterns altogether. This is not the case, however, with modes I and II, where the priority of the tip in attracting the stress field is overwhelming. These cracks do not appear to roughen on the large scales even with quenched disorder.

In summary, we believe that the experimental observations pose an interesting riddle whose resolution will need a careful assessment of the experimental conditions and their inclusion in the theory. It is our hope that the solution presented above will turn out to be a useful tool in achieving this goal.

ACKNOWLEDGMENTS

We thank Jean-Pierre Eckmann for useful discussions on Fourier transforms in the vicinity of branch cuts. F.B. thanks the ‘‘Fundacion Andes’’ and the program ‘‘Inicio de Carrera para Jovenes Cientificos’’ (Grant No. C-13760). This work was supported in part by the Petroleum Research Fund, The European Commission under the TMR program and the Naftali and Anna Backenroth-Bronicki Fund for Research in Chaos and Complexity. A.L. was financially supported by the Minerva Foundation, Munich, Germany.

[1] L.D. Landau and E.M. Lifshitz, *Theory of Elasticity*, 3rd ed. (Pergamon, London, 1986).
[2] N.I. Muskhelishvili, *Some Basic Problems in the Mathematical Theory of Elasticity* (Noordhoff, Groningen, 1952).
[3] H.J. Herrmann and S. Roux, *Statistical Models for the Fracture of Disordered Media* (North-Holland, Amsterdam, 1990), and references therein.
[4] J. Fineberg and M. Marder, Phys. Rep. **313**, 1 (1999), and references therein.
[5] L.B. Freund, *Dynamic Fracture Mechanics* (Cambridge University Press, Cambridge, 1998).
[6] M. Barber, J. Donley, and J.S. Langer, Phys. Rev. A **40**, 366 (1989).
[7] See for example, J. Kertész in Ref. [3].
[8] E. Louis and F. Guinea, Europhys. Lett. **3**, 871 (1987).
[9] See, for example, Ref. [4], Sec. II C. There is no universal agreement on the experimental velocity law, and other choices can be made here.
[10] F. Barra, B. Davidovitch, A. Levermann, and I. Procaccia, Phys. Rev. Lett. **87**, 134501 (2001).
[11] F. Barra, B. Davidovitch, and I. Procaccia, Phys. Rev. E (to be published), e-print cond-mat/0105608.
[12] F. Barra, H.G.E. Hentschel, A. Levermann, and I. Procaccia, Phys. Rev. E **65**, R045101 (2002).
[13] S. Ramanathan, D. Ertaş, and D.S Fisher, Phys. Rev. Lett. **79**, 873 (1997).
[14] M.B. Hastings and L.S. Levitov, Physica D **116**, 244 (1998).
[15] B. Davidovitch, H.G.E. Hentschel, Z. Olami, I. Procaccia, L.M. Sander, and E. Somfai, Phys. Rev. E **59**, 1368 (1999).
[16] Z. Olami, I. Procaccia, and R. Zeitak, Phys. Rev. E **52**, 3402 (1995).
[17] E. Bouchaud, J. Phys.: Condens. Matter **9**, 4319 (1997).
[18] A. Parisi, G. Caldarelli, and L. Pietronero, e-print cond-mat/0004374.
[19] B. Cottrell and J.R. Rice, Int. J. Fract. **16**, 155 (1980).
[20] E. Bouchaud, J.P. Bouchaud, D.S. Fisher, S. Ramanathan, and J.R. Rice, J. Mech. Phys. Solids **50**, 1703 (2002).